Microwave Antenna Holography

David J. Rochblatt, *Member, IEEE,* and Boris L. Seidel, *Member, IEEE*

Abstract—**Microwave holography, as applied to reflector antennas, is a technique with utilizes the Fourier Transform relation between the complex far-field radiation pattern of an antenna and the complex aperture distribution. Resulting aperture phase and amplitude distribution data are used to precisely characterize various crucial performance parameters, including panel alignment, subreflector position, antenna aperture illumination, directivity at various frequencies, and gravity deformation effects. The holography technique provides a methodology for analysis, evaluation, and RF performance improvement of large reflector and beam waveguide antennas. Strong CW signals obtained from geostationary sources were used as far-field sources. This article describes the application of the holography technique to the newly constructed NASA/JPL Deep Space Network (DSN) 34-m beam-waveguide antenna, resulting in 4.1-dB performance improvement at 32 GHz by reducing the main reflector rms surface error to 0.43 mm. The improved antenna performance was verified by additional holographic measurements and efficiency measurements at *X*-band (8.45 GHz). Microwave holography has been demonstrated to be a required tool for achieving antenna aperture efficiency of 52% at *Ka*-band (32 GHz), and is likely required for maintaining an operational DSN *Ka*-band ground antenna capability.**

Introduction

MICROWAVE holography is a measurement technique that has now been applied to all of the 34-m High Efficiency (HEF) and 70-m antennas in the DSN. The raw data (the observable) for this technique is the complex far-field pattern of the antenna under test. Recently, the holographic technique was applied to the new DSN 34-m beam-waveguide (BWG) antenna (DSS 13). Measurements were made from the Cassegrain (f1) focus of the antenna to optimize the subreflector position, evaluate the antenna main reflector, and to reset the surface as necessary. Fig. 1 shows the new DSS 13 antenna with the *Ku*-band front-end test package [1] mounted at the Cassegrain focus (f1). Measurements were made at several elevation angles to aid in the study of structural deformation due to gravitational effects.

A narrow bandwidth data acquisition system was loaned to JPL by Eikontech Ltd., (Sheffield, England) to perform the measurement. The data reduction and analysis was entirely done using the JPL-developed (Rochblatt) algorithms.

Manuscript received June 13, 1991; revised October 11, 1991. The research described in this paper was carried out at the Jet Propulsion Laboratory, California Institute of Technology, under a contract with the National Aeronautics and Space Administration.

The authors are with the Jet Propulsion Laboratory, California Institute of Technology, 4800 Oak Grove Drive, Pasadena, CA 91109.

IEEE Log Number 9107461.

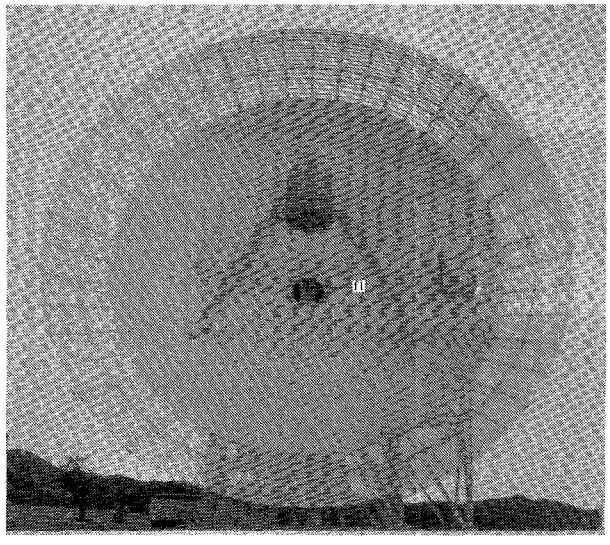

Fig. 1. DSS 13 34-meter beam-waveguide antenna showing the *Ku*-band horn feed at the f1 position at the Cassegrain focus.

Many useful measurements were made. The subreflector position was verified. Information obtained from the JPL analysis algorithms was successfully applied and substantially reduced the rms surface error of the optically set main reflector. The final holographically set main reflector surface is better than the specification and exceeds the goal set by the project requirements.

Mathematical Algorithms

The mathematical relationship between an antenna far-field radiation pattern (T) and the antenna surface-induced current distribution (J) is given by

$$\vec{T}(u, v) = \iint_S \tilde{J}(x', y') \exp(jkz') \cdot [\exp[-jkz'(1 - \cos\theta)]] \cdot \exp[jk(ux' + vy')]\, dx'\, dy' \quad (1)$$

where

$z^1(x^1, y^1)$: Defines the surface S.
u, v: Direction cosine space.
θ: Observation angle.

For a small angular extent of the far-field pattern, this expression reduces to

$$\vec{T}(u, v) = \iint_S \tilde{J}(x', y') \exp(jkz') \cdot \exp[jk(ux' + vy')]\, dx'\, dy' \quad (2)$$

Equation (2) is an exact Fourier Transform of the induced surface current. To derive the residual surface error, geometrical optics ray tracing is used to relate the normal error, ϵ, to the axial error and phase in a main reflector paraboloid geometry (Fig. 2):

$$1/2\ \Delta PL = 1/2\ [P'P + PQ]$$

$$= 1/2 \left[\frac{\epsilon}{\cos \varphi} + \frac{\epsilon \cos 2\varphi}{\cos \varphi} \right]$$

$$= \epsilon \cos \varphi \tag{3}$$

$$\text{Phase } (\Delta PL) = \frac{4\pi}{\lambda} \epsilon \cos \varphi \tag{4}$$

and

$$\cos \varphi = \frac{1}{\sqrt{1 + \dfrac{X^2 + Y^2}{4F^2}}} \tag{5}$$

F: Focal length.

Allowing for the removal of a constant phase term and substituting (4) into (2) yields:

$$T(u, v) = \exp(-j2kF) \iint_S |\tilde{J}(x', y')|$$

$$\cdot \exp\left(j4\pi \frac{\epsilon}{\lambda} \cos \varphi\right)$$

$$\cdot \exp\left[jk(ux' + vy')\right] dx'\, dy'. \tag{6}$$

For the processing of sampled data, the associated Discrete Fourier Transform (DFT) is utilized:

$$T(p\Delta u, q\Delta v) = sx\ sy \sum_{n=-N1/2}^{N1/2-1} \sum_{m=-N2/2}^{N2/2-1} J(nsx, msy)$$

$$\cdot \exp\left[j2\pi\left(\frac{np}{N1} + \frac{mq}{N2}\right)\right]. \tag{7}$$

Where

$N1 \times N2$	is the measured data array size.
sx, sy:	sampling intervals on the aperture coordinates.
n, m, p, q:	Integers indexing the discrete samples.
Δu, ΔV:	Sampling interval in the U, V far-field space.

Since the magnitude of the far-field pattern is essentially bounded, the Fast Fourier Transform (FFT) is usually used for computation, and symbolized here by (F). Solving for the residual normal surface error and substituting (5), we obtain:

$$\epsilon(x, y) = \frac{\lambda}{4\pi} \sqrt{1 + \frac{x^2 + y^2}{4F^2}}$$

$$\cdot \text{Phase}\left[\exp(j2kF) F^{-1}[T(u, v)]\right]. \tag{8}$$

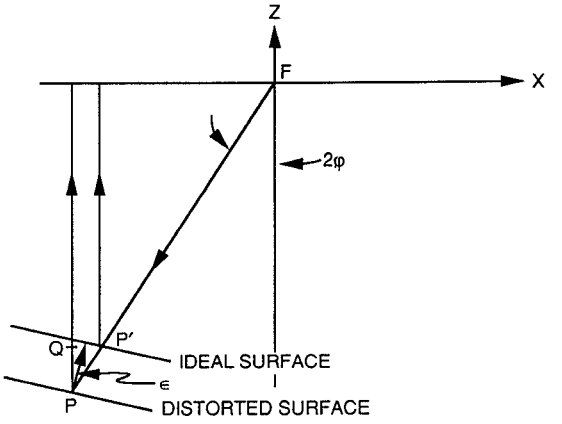

Fig. 2. Surface distortion geometry.

The spatial resolution in the final holographic maps is defined [2]:

$$\delta = \frac{D}{kN} \tag{9}$$

where:

D:	Main reflector diameter
N:	The square root of the total number of data points
k:	Sampling factor, usually $0.5 < k < 1.0$.

The accuracy in each resolution cell of the final holographic maps is [3]:

$$\sigma \cong .082 \frac{\lambda D}{\delta\ \text{SNR}} \tag{10}$$

where:

λ:	Wavelength
SNR:	Beam peak voltage signal-to-noise ratio.

The resulting aperture function needs to be corrected for modulo-2π phase errors, and a global least-squares fit perform on the data to the "best-fit" paraboloid. This process also allows for the correction of antenna pointing errors introduced during the measurement. The "best-fit" paraboloid is found by minimizing S, the sum squares of the residual path length changes:

$$S = \sum_{i=1}^{N^2} \Gamma_{(\text{DSS-13})} (\Delta PL_i)^2 A_i \tag{11}$$

where:

$\Gamma_{(\text{DSS13})}$:	DSS 13 support domain constraints masking operator
ΔPL_i:	Path length change
A_i:	Amplitude weighting factor

with respect to 6 degrees-of-freedom of the reflector motion; three vertex translations, two rotations, and a focal length change. The six partial differential equations, which are solved simultaneously, are of the form:

$$\frac{\partial S}{\partial \text{Par}} = 2 \sum_{i=1}^{N^2} \Gamma_{(\text{DSS13})} \frac{\partial \Delta PL_i}{\partial \text{Par}} \Delta PL_i A_i = 0 \tag{12}$$

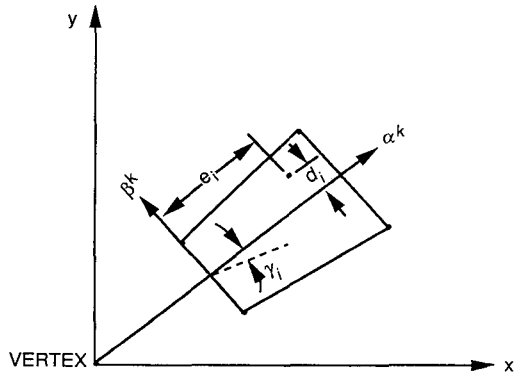

Fig. 3. Rigid body panel motion modeling.

where:

Par: One parameter of the 6 degrees-of-freedom.

It is correct to apply the best-fit paraboloid algorithm to either the conventional cassegrain paraboloid-hyperboloid or dual-shaped reflector systems even though the latter do not use a paraboloid as the main reflector. Either design is a planewave-to-point source transformer, differing only in the field intensity distribution. The resultant aperture function at the end of this process is referred to as "Effective Map" since it includes all phase effects that are contributing to the antenna performance [4]. These effects include the subreflector scattered (frequency-dependent) feed phase function. Removal of the feed phase function and subreflector support structure diffraction effects results in a frequency independent map, which is referred to below as the "Mechanical Map."

Panel setting information is derived by sorting together all the data points within each panel and performing a least squares fit. The agorithms allow for one translation and two rotations, S^k, α^k, β^k, hence a rigid body motion. For each panel and its associated n data points we solve for the motion parameters via (Fig. 3):

$$\begin{bmatrix} \sum_{i=1}^{n} \cos^2(\gamma_i) & \sum_{i=1}^{n} d_i * \cos^2(\gamma_i) & -\sum_{i=1}^{n} e_i * \cos(\gamma_i) \\ \sum_{i=1}^{n} d_i * \cos^2(\gamma_i) & \sum_{i=1}^{n} d_i^2 * \cos^2(\gamma_i) & -\sum_{i=1}^{n} e_i * d_i * \cos(\gamma_i) \\ -\sum_{i=1}^{n} e_i * \cos(\gamma_i) & -\sum_{i=1}^{n} d_i * e_i * \cos(\gamma_i) & \sum_{i=1}^{n} e_i^2 \end{bmatrix} \begin{bmatrix} S^k \\ \alpha^k \\ \beta^k \end{bmatrix} = \begin{bmatrix} -\sum_{i=1}^{n} \epsilon_i * \cos^2(\gamma_i) \\ \sum_{i=1}^{n} \epsilon_i * d_i * \cos^2(\gamma_i) \\ \sum_{i=1}^{n} \epsilon_i * e_i * \cos(\gamma_i) \end{bmatrix}. \quad (13)$$

This mathematical process also increases the accuracy in determining the screw adjustment correction by a factor of $\sqrt{n}$.

Holographic Measurements and Results

In August and September of 1990, four successful holography measurements were made from the f1 focus of the new DSS 13 BWG antenna. Strong CW signals obtained from geostationary satellite beacons were used as far-field sources. Three different geostationary satellites were successfully scanned, producing successful high- and medium-resolution data sets at elevation angles of 46.5 degrees, 37 degrees, and 12.7 degrees. The measurements obtained provided the necessary subreflector position information, panel setting information, a look at the adjusted surface of the antenna, and information about the gravity performance of the structure at a low elevation angle. The holographic antenna measurements used satellite signal and ephemeris information supplied by several commercial companies. The cooperation received from GTE (GSTAR W103), GE (SatComm K1), and ComSat (Intelsat V) is thoroughly appreciated and gratefully acknowledged.

The results of the four successful high- and medium-resolution scans are reported here. Scan JPL106 was a high-resolution scan that provided the first high-resolution look at the surface of the optically set antenna as well as subreflector position error. This is the scan that was used for deriving the required panel setting information. Scan JPL110 was also a high-resolution scan and provided the after-adjustment look at the surface of the antenna. Scans JPL113 and JPL123 provided surface maps of the antenna at two additional elevation angles (37 degrees and 12.7 degrees, respectively). The last scan, JPL123 at 12.7-degrees elevation, provides valuable information for the structural modeling specialists. These four scans are summarized in Table I.

It is known that the indicated rms error of the antenna surface is affected by the weakly illuminated outer portion of the dish. When the outer edge of the antenna is included in the analysis, the calculated surface rms error is larger than that obtained from analysis of the strongly illuminated portion of the dish.

Functionally, the outer 0.6 meter of the antenna is little more than a noise shield. The rms error obtained from analysis of the central 32 meters of the antenna is therefore more representative of the actual surface than the rms obtained from examination of the full 34-m dish. The rms values for both the full and the central 32 meters of the antenna are included in Table I. It is estimated that the 1-sigma error of the rms (central 32 meters) is approximately ± 0.05 mm.

The holographic measurement program at DSS 13 started with measurements taken at an elevation angle of about 46.5 degrees. High-resolution scan JPL106 sup-

TABLE I
RESULTS OF DSS 13 MICROWAVE HOLOGRAPHY AT f1

Scan	JPL106	JPL110	JPL113	JPL123
Satellite	GSTAR W103	GSTAR W103	SatComm K1	Intelsat V
Elevation Angle	46.5	46.5	37.0	12.7
Measurement Frequency, GHz	12.198	12.198	12.198	11.701
Surface	Mech	Mech	Mech	Eff*
Array Size	127 × 127	127 × 127	127 × 127	51 × 51
Resolution, m	0.32	0.32	0.32	0.80
RMS, mm				
Surface Normal				
Full Antenna	1.07	0.58	0.71	0.66
Central 32-m	0.88	0.45	0.43	0.50
Axial				
Central 32-m	0.77	0.39	0.37	0.43
Infinite Res	0.83	0.42	0.40	0.50
Estimated Surface Error Loss, dB				
Ruze				
2.30 GHz	0.028	0.007	0.006	0.010
8.45 GHz	0.375	0.096	0.087	0.136
32.00 GHz	5.375	1.376	1.248	1.951
Estimated Subreflector Position Error, mm				
X	−0.53	+0.28	+1.07	−1.88
Y	−1.06	−1.41	−3.07	−4.72
Z	+1.10	+1.13	+0.66	+0.39

* Eff: effective surface error map without removal of the feed/subreflector phase function.

plied the data required for verifying the subreflector position, analyzing the antenna surface, and providing the panel setting information. The surface images derived from the aperture plane phase represent the antenna surface deviations from ideal in the surface normal direction. In the images, the subreflector, the tripod and its shadows, and the bypass beam waveguide are intentionally masked out. The remaining surface is overlaid with an outline of each reflecting panel. The surface error information is shown in pseudo color, with red and blue indicating the high and low deviations, respectively. Fig. 4 shows the surface error map of the central 32 meters of the DSS 13 antenna surface as found on August 28, 1990 by scan JPL106. The main reflector surface normal rms error was found to be 0.88 mm (0.77-mm axial) at a resolution of 0.32 meters.

The indicated rms increases as the lateral resolution of the measurement increases. This is an expected result as there is less area averaging occurring as the resolution increases. The asymptotic or infinite resolution rms can be estimated by analyzing the scan data at varying resolutions.

It is estimated that the rms error found by holography high-resolution (0.32-meter) scans is 8% below the infinite resolution rms. That estimate will be used here for consistency. (Since scan JPL123 (12.7-degree elevation)

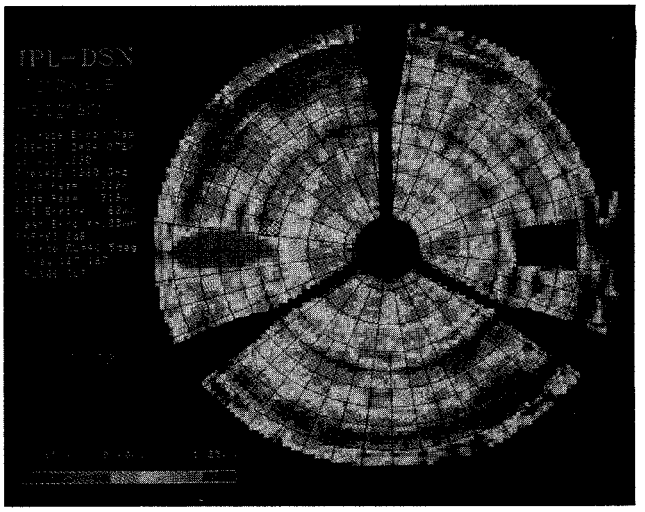

Fig. 4. High resolution (0.32-meter) error map of the central 32 meters of the DSS 13 antenna surface at 46-degrees elevation, before panel setting, as derived from scan JPL106 (August 28, 1990). The normal, axial, and infinite resolution axial rms errors are 0.88 mm, 0.77 mm, and 0.83 mm, respectively.

was taken at medium (0.80-meter) resolution, a 16% correction is applied to this one scan.)

Fig. 5 shows the predicted surface error map representing the best achievable surface that would have resulted if the 1716 screws were adjusted precisely as specified by the software. The surface normal rms of this predicted antenna is 0.36 mm at a resolution of 0.32 meter. The image reveals that the panels in the outer two rings are over-bent. Note that the present software moves panels as rigid bodies and that further improvements would be possible by unbending individual panels.

The panel setting information derived from scan JPL106 was applied to the surface panel adjusting screws. As a scheduling expedient, it was decided to adjust the surface panels by turning the adjusting screws to the nearest $1/8$ of a turn (0.16 mm). Screws requiring adjustment of less than $\pm 1/8$ of a turn were not touched.

The surface error map shown in Fig. 6 was measured on September 7, 1990 after panel resetting (scan JPL110). The over-bent panels in rings 8 and 9, as well as many of the other predicted features, are clearly confirmed. The rms surface error achieved by holography-based panel adjustment is 0.45-mm surface normal (0.39-mm axial) at a resolution of 0.32 meters. This is equivalent to an infinite resolution axial rms error of 0.42 mm. This rms error not ony exceeds the specification, it also exceeds the project goal. A higher-than-normal noise level in scan JPL110 leads us to believe that the achieved rms surface error is actually somewhat lower than indicated by this measurement. Indeed, scan JPL113 (Fig. 7), taken at a 37-degree elevation angle, reveals a surface normal rms error of 0.43 mm and an axial error of 0.37 mm giving an infinite resolution axial error of 0.40 mm. Efficiency measurements indicate the 45-degree rigging angle surface to be better than the 37-degree elevation angle surface. We therefore conclude that, at the rigging angle, the holographically set

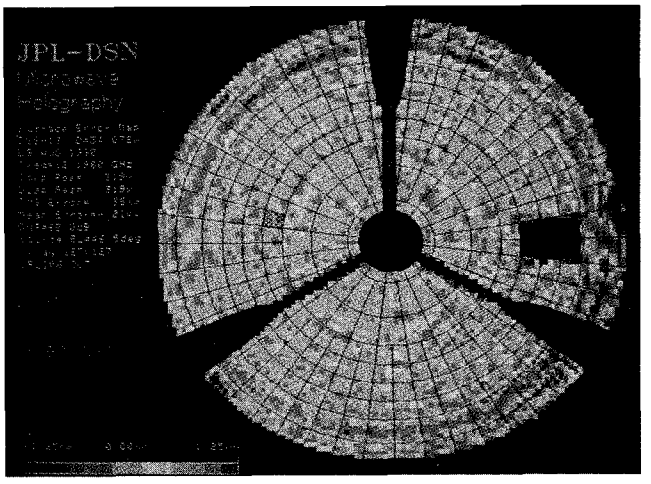

Fig. 5. Predicted surface error map derived from scan JPL 106. This represents the best achievable rigging angle surface that would have resulted if the 1716 screws were adjusted precisely as specified by the software. The predicted normal, axial, and infinite resolution axial rms errors are 0.36 mm, 0.31 mm, and 0.33 mm, respectively.

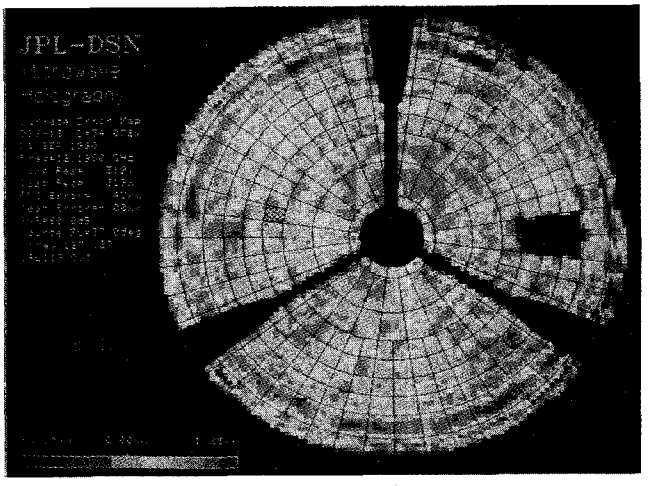

Fig. 7. High resolution (0.32-meter) error map of the central 32-meters of the DSS 13 antenna surface at 37-degrees elevation, after panel setting, as derived from scan JPL113 (September 11, 1990). The normal, axial, and infinite resolution axial rms errors are 0.43 mm, 0.37 mm, and 0.40 mm, respectively.

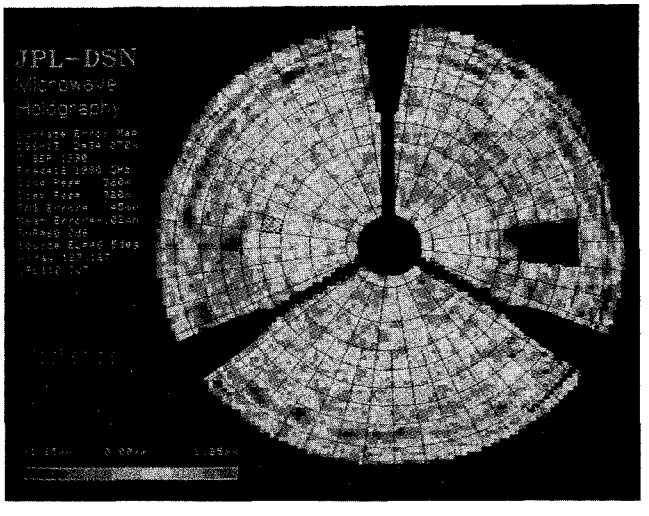

Fig. 6. High resolution (0.32-meter) error map of the central 32 meters of the DSS 13 antenna surface at 46-degrees elevation, after panel setting, as derived from scan JPL110 (September 7, 1990). The normal, axial, and infinite resolution axial rms errors are 0.45 mm, 0.39 mm, and 0.42 mm, respectively.

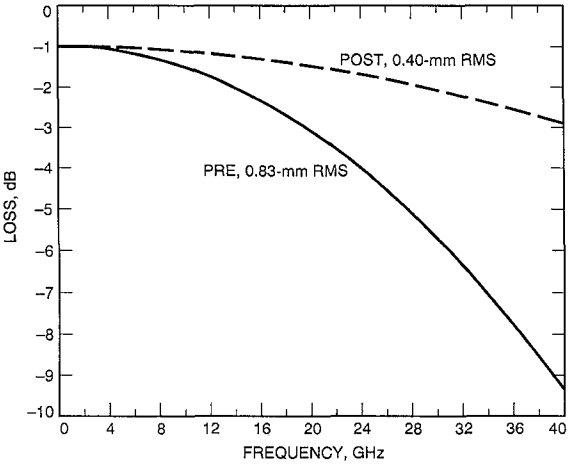

Fig. 8. Loss due to surface error versus frequency. The loss indicated in these curves is based on aperture blockage and surface roughness. No attempt was made to include I^2R losses. An estimated improvement in antenna performance of approximately 4.1 dB was achieved at 32 GHz after panel resetting.

antenna surface actually has an infinite resolution axial rms error of slightly less than 0.40 mm.

As shown in Fig. 8, the post-holography surface provides a performance improvement of about 0.2 dB at 8.45 GHz, increasing to 4.1 dB at 32 GHz. The DSS 13 surface specifications, along with the corresponding efficiency calculations and measurements, are summarized in Table II.

Tables III through VI contain *X*-band and *Ka*-band calculations of antenna efficiency. The results are obtained by applying Ruze factors [5] to the holography-obtained axial rms surface error[1] values along with other known blockages and losses. These calculated efficiencies are compared to the radiometrically obtained measurements of efficiency.

The surface error map shown in Fig. 9 was derived from medium-resolution (0.80-meter) holography measurements made on September 18, 1990 at an elevation angle of 12.7 degrees (scan JPL123). The surface normal rms error at this low elevation angle and resolution is 0.50 mm. The corresponding axial and infinite resolution axial rms errors are 0.43 mm and an estimated 0.50 mm, respectively.

The holography measurements indicate that the subreflector is displaced from the optimum position by 5 mm laterally and 0.4 mm axially at the 12.7-degree elevation angle (see Table I). A Physical Optics analysis computation reveals 0.25 dB of performance loss at 32 GHz for this amount of subreflector displacement. Adding this 0.25 dB of performance loss to the measured 39.4% antenna efficiency results in a computed performance of 41.7% at

[1]The axial rms surface errors are equal to the half pathlength errors in the familiar form of the Ruze gain-degradation factor $k_g = \exp - [4 * \pi * \epsilon/\lambda]^2$. In this expression, ϵ is the half pathlength error and λ is the wavelength.

TABLE II
DSS 13 RIGGING ANGLE SURFACE SPECIFICATIONS, EFFICIENCY CALCULATIONS AND MEASUREMENTS

Antenna Surface	mm RMS	Calculated/Measured Aperture Efficiency, Percent	
		8.45 GHz	32.0 GHz
As Found	0.83	71.7/71.9	21.6
Specified	0.61	74.6	38.3
Goal	0.43	76.4	53.6
After Reset	0.40	76.6/75.4	56.0/52.3
Potential	0.36	76.9	59.2

Notes:
1) Efficiency estimates include 0.07-dB I^2R loss at 8.45 GHz and 0.27-dB I^2R loss at 32 GHz.
2) Both the 8.45-GHz and the 32-GHz efficiency estimates include 186.6 m^2 of aperture blockage.
3) The measured efficiency values (supplied by Slobin Ref. 5) are derived from radiometric measurements.
4) Given a perfect main reflector surface, the estimated *X*- and *Ka*-band efficiencies would be 78.2% and 74.7%, respectively. This difference is due to the different I^2R loss at the two frequencies.

TABLE III
COMPARISON OF HOLOGRAPHY-BASED EFFICIENCY ESTIMATE WITH MEASURED VALUE. *X*-BAND POST ADJUSTMENT AT RIGGING ANGLE (USING THE 37-DEGREE INFINITE RESOLUTION RMS VALUE)

DSS 13 34-meter BWG Antenna
8.45 GHz @ 46-degrees Elevation

Gross Area	907.9 m^2
Less	
Noise Shield	64.7 m^2
Blockage	9.0 m^2
Strut Blockage	74.4 m^2
Bypass Blockage	23.5 m^2
Illumination Taper	15.0 m^2
Subtotal	186.6 m^2
Ruze Loss (0.40-mm)	14.3 m^2
Position Loss	negligible
Subtotal Effective Area	707.0 m^2
I^2R Loss, *X*-Band (0.07-dB)	11.3 m^2
Net Effective Area	695.7 m^2
Area Efficiency	
Estimated	76.6%
Measured	75.4%

TABLE IV
COMPARISON OF HOLOGRAPHY-BASED EFFICIENCY ESTIMATE WITH MEASURED VALUE. *X*-BAND POST ADJUSTMENT AT 12.7 DEGREES.

DSS 13 34-meter BWG Antenna
8.45 GHz @ 12.7 degrees

Gross Area	907.9 m^2
Less	
Noise Shield	64.7 m^2
Blockage	9.0 m^2
Strut Blockage	74.4 m^2
Bypass Blockage	23.5 m^2
Illumination Taper	15.0 m^2
Subtotal	186.6 m^2
Ruze Loss (0.50 mm)	22.2 m^2
Position Loss	negligible
Subtotal Effective Area	699.1 m^2
I^2R Loss, *X*-Band (0.07-dB)	11.2 m^2
Net Effective Area	687.9 m^2
Area Efficiency	
Estimated	75.8%
Measured	74.0%

TABLE V
COMPARISON OF HOLOGRAPHY-BASED EFFICIENCY ESTIMATE WITH MEASURED VALUE. *Ka*-BAND POST ADJUSTMENT AT RIGGING ANGLE (USING THE 37-DEGREE INFINITE RESOLUTION RMS VALUE).

DSS 13 24-meter BWG Antenna
32 GHz @ Rigging Angle

Gross Area	907.9 m^2
Less	
Noise Shield	64.7 m^2
Blockage	9.0 m^2
Strut Blockage	74.4 m^2
Bypass Blockage	23.5 m^2
Illumination Taper	15.0 m^2
Subtotal	186.6 m^2
Ruze Loss (0.40 mm)	180.2 m^2
Position Loss	negligible
Subtotal Effective Area	541.1 m^2
I^2R Loss, *Ka*-Band (0.27-dB)	32.6 m^2
Net Effective Area	508.5 m^2
Area Efficiency	
Estimated	56.0%
Measured	52.3%

TABLE VI
COMPARISON OF HOLOGRAPHY-BASED EFFICIENCY ESTIMATE WITH MEASURED VALUE. *Ka*-BAND POST ADJUSTMENT AT 12.7 DEGREES.

DSS 13 34-meter BWG Antenna
32 GHz @ 12.7 degrees

Gross Area	907.9 m^2
Less	
Noise Shield	64.7 m^2
Blockage	9.0 m^2
Strut Blockage	74.4 m^2
Bypass Blockage	23.5 m^2
Illumination Taper	15.0 m^2
Subtotal	186.6 m^2
Ruze Loss (0.50 mm)	261.0 m^2
Position Loss (0.25-dB)	25.7 m^2
Subtotal Effective Area	434.6 m^2
I^2R Loss, *Ka*-Band (0.27-dB)	26.2 m^2
Net Effective Area	408.4 m^2
Area Efficiency	
Estimated	45.0%
Measured	39.4%

this elevation angle. The 1-sigma error bars on the measured and estimated 32 GHz efficiency values overlap given a 5-mm subreflector error, an estimated uncertainty in surface rms error of ± 0.05 mm, and assuming a 5% accuracy for the radiometric measurements.

FUTURE WORK

The holographically set antenna surface already exceeds the specification set forth in the project requirements. However, fine tuning the main reflector surface will yield at least another 0.25 dB of improved *Ka*-band (32-GHz) performance. Careful subreflector positioning might provide another 0.25 dB of performance at low elevation angles. When developed and applied, panel unbending techniques will further improve aperture efficiency.

It is also necessary to return to DSS 13 to make measurements at the beam waveguide focus that were not obtained in the initial development phase. Information obtained from these measurements, when differenced from

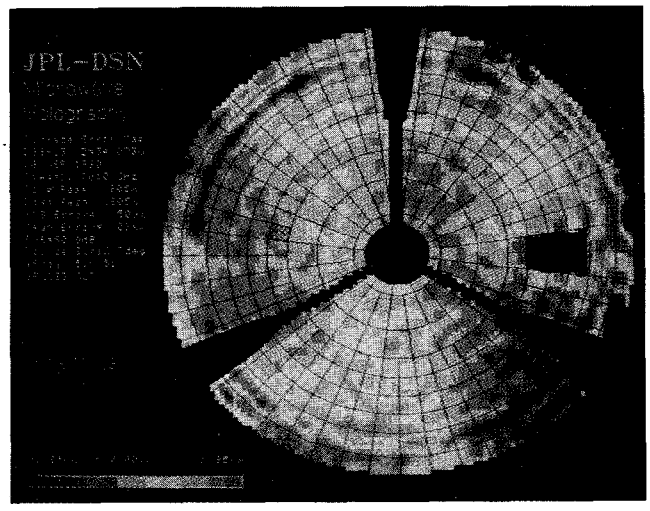

Fig. 9. Medium-resolution (0.80-meter) error map of the central 32 meters of the DSS 13 antenna surface at 12.7-degrees elevation, after panel setting, as derived from scan JPL123 (September 18, 1990). The normal, axial, and infinite resolution axial rms errors are 0.50 mm, 0.43 mm, and 0.50 mm, respectively.

those obtained at f1, will provide an important holographic diagnosis of the BWG effects on the antenna system.

Finally, we plan to provide a measurement system for aligning and maintaining all of the deep space tracking antennas in the NASA/JPL worldwide network. Such a system is indispensable to an operational *Ka*-band ground antenna capability in support of future deep space missions. Microwave holography provides a time and cost effective means for providing this support.

Conclusion

In conclusion, the principal f1 holography goal of obtaining a rigging angle surface rms error of 0.5 mm, or better, at DSS 13 has been met. The JPL-developed holography algorithms, the RF test package, and the concept (and execution) of f1 holography measurements on a BWG antenna worked extremely well. JPL microwave holography enabled reducing the surface error of the DSS 13 antenna from the optically set, as-found 0.83-mm axial rms error down to a very respectable 0.40-mm rms. This holographically improved surface not only exceeds the specification (0.61 mm), but also exceeds the 0.43-mm goal. The holographically set antenna surface provides an additional 4.1 dB of performance at 32 GHz. Even better results can be obtained in the future given another pass of holography adjustments along with some panel unbending.

Acknowledgment

The authors wish to thank Manuel Franco from JPL and Paul Wright and Eric Schoessow from Eikontech Ltd. for helping with the holographic measurements.

References

[1] T. Y. Otoshi, S. R. Stewart, and M. M. Franco, "A portable *Ku*-band front-end test package for beam-waveguide antenna performance evaluation," TDA Progress Report 42-107, Jet Propulsion Laboratory, Pasadena, CA, Nov. 15, 1991.

[2] D. J. Rochblatt and B. L. Seidel, "DSN microwave antenna holography," TDA Progress Report 42-76, Jet Propulsion Laboratory, Pasadena, CA, pp. 27–42, 1983.

[3] D. J. Rochblatt and Y. Rahmat-Samii, "Effects of measurement errors on microwave antenna holography," *IEEE Trans. Antennas Propagat.*, July 1991.

[4] D. J. Rochblatt, Y. Rahmat-Samii, and J. H. Mumford, "DSN microwave antenna holography part II: Data processing and display of high resolution effective maps," TDA Progress Report 42-87, Jet Propulsion Laboratory, Pasadena, CA, pp. 92–97, 1986.

[5] J. Ruze, "Antenna tolerance theory—a review," *Proc. IEEE*, vol. 54, pp. 663–640.

[6] A. P. Anderson, J. C. Bennett, A. J. T. Whitaker, and M. P. Godwin, "Measurement and optimization of a large reflector antenna by microwave holography," *Proc. Int. Conf. on Ant. and Prop.*, IEE Publication no. 169, pp. 128–131, London, England, 1978.

[7] P. F. Scott and M. Ryle, "A rapid method for measuring the figure of a radio telescope reflector," *Mon. Not. Roy. Astr. Soc.*, vol. 178, pp. 539–545, 1977.

[8] D. J. Rochblatt, "System analysis for DSN microwave antenna holography," TDA Progress Report 42-97, Jet Propulsion Laboratory, Pasadena, CA, pp. 132–157, 1988.

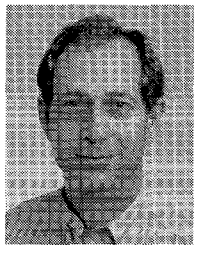

David J. Rochblatt (S'81–M'82) served in the Israeli Defence Forces from 1971 to 1974. He received the B.S. Magna Cum Laude, and M.S. degrees in Electrical Engineering, both from the University of California Los Angeles (UCLA), in 1978 and 1980 respectively.

From 1978 he designed analog and digital circuits including VLSI chips and microprocessor based systems for consumer, industrial, and medical electronics industries including security systems, camera automatic focusing systems, remote control RF actuators and image enhancement systems for medical applications. He served on the Scientific Advisory Committee of Save A Heart Foundation, Cardiology Department of Cedar Sinai Medical Center. He has been a consultant to several industrial and aerospace companies. He joined the NASA Jet Propulsion Laboratory/California Institute of Technology, in 1981. As a group leader for the Tracking Systems and Applications Section he was responsible for the design of the front-end microwave subsystems for mobile Very Long Baseline Interferometer (VLBI) station hardware. This included the design of dual-frequency Cassegrainian reflector antennas, and low-noise GaAs FET receiver amplifiers. In the Antenna and Microwave Development Group he was a member of the team that designed the new NASA 70-meter antennas for the Deep Space Network (DSN). He is the principal developer of NASA-JPL DSN microwave antenna holography, a technique which provides a methodology for the analysis, evaluation, and performance improvement of large reflector and beam waveguide antennas. Most recently he was a member of the imaging team that helped to characterize the flawed Hubble Space Telescope primary mirror using phase retrieval holography.

Mr. Rochblatt is a member of Tau Beta Pi and Eta Kappa Nu.

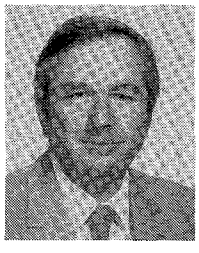

Boris L. Seidel (M'63) was born in Chicago, IL on May 29, 1936. He received the B.S. and M.S. degrees in electrical engineering in 1961 and 1962, respectively, from the University of Illinois, Urbana.

Since 1962 he has worked in the Telecommunications Division of the Jet Propulsion Laboratory, California Institute of Technology, Pasadena, CA. His duties have included the development of specialized ground based receiving systems for radio science investigations in the NASA deep space program. He has also served as a radio science coinvestigator on several NASA and cooperative USA/European deep space missions. He has worked with the radio astronomy community and participated in the first trans-Pacific interferometer experiments conducted between the NASA Goldstone, California and the Australian Deep Space Tracking Complexes. He has worked in applying radio astronomical techniques to the calibration of large antennas. His present work is in the area of microwave imaging of large aperture antenna main reflector surfaces for purposes of improving RF performance at high frequencies.

Mr. Seidel holds one United States patent for an antenna feed system matched to receive circular polarization while transmitting linear polarization and has received several NASA new technology awards. He is a member of Tau Beta Pi, Eta Kappa Nu, Sigma Tau, and Sigma Xi.